Available online at www.sciencedirect.com
ScienceDirect
Journal of Computational Physics 220 (2006) 155–174
JOURNAL OF COMPUTATIONAL PHYSICS
www.elsevier.com/locate/jcp

Accurate multiscale finite element methods for two-phase flow simulations

Y. Efendiev [a,*], V. Ginting [b], T. Hou [c], R. Ewing [d]

[a] Department of Mathematics, Texas A&M University, College Station, TX 77843-3368, United States
[b] Institute for Scientific Computation and Department of Mathematics, Texas A&M University, College Station, TX 77843-3368, United States
[c] Applied Mathematics, Caltech, Pasadena, CA 91125, United States
[d] Institute for Scientific Computation and Department of Mathematics, Texas A&M University, College Station, TX 77843-3368, United States

Received 10 February 2005; received in revised form 28 January 2006; accepted 5 May 2006
Available online 10 July 2006

Abstract

In this paper we propose a modified multiscale finite element method for two-phase flow simulations in heterogeneous porous media. The main idea of the method is to use the global fine-scale solution at initial time to determine the boundary conditions of the basis functions. This method provides a significant improvement in two-phase flow simulations in porous media where the long-range effects are important. This is typical for some recent benchmark tests, such as the SPE comparative solution project [M. Christie, M. Blunt, Tenth spe comparative solution project: a comparison of upscaling techniques, SPE Reser. Eval. Eng. 4 (2001) 308–317], where porous media have a channelized structure. The use of global information allows us to capture the long-range effects more accurately compared to the multiscale finite element methods that use only local information to construct the basis functions. We present some analysis of the proposed method to illustrate that the method can indeed capture the long-range effect in channelized media.

Keywords: Multiscale; Finite element; Finite volume; Global; Two-phase; Upscaling

1. Introduction

Subsurface flows, as occur in the production of hydrocarbons as well as in environmental remediation projects, are affected by heterogeneities in a wide range of length scales. It is, therefore, very difficult to resolve numerically all of the scales that impact transport through such systems. Typically, upscaled or multiscale models are employed for such systems. The main idea of upscaling techniques is to form coarse-scale equations with a prescribed analytical form that may differ from the underlying fine-scale equations. In multiscale

* Corresponding author. Tel.: +1 979 845 1972.
E-mail address: efendiev@math.tamu.edu (Y. Efendiev).

0021-9991/$ - see front matter © 2006 Elsevier Inc. All rights reserved.
doi:10.1016/j.jcp.2006.05.015

methods, the fine-scale information is carried throughout the simulation and the coarse-scale equations are generally not expressed analytically, but rather formed and solved numerically.

Our purpose in this paper is to propose a modified multiscale finite element method (MsFEM) for the computations of two-phase flows. MsFEM is first introduced in [18]. Its main idea is to incorporate the small-scale information into finite element basis functions and capture their effect on the large scale via finite element computations. Recently, a number of multiscale numerical methods, such as residual free bubbles [6,23], variational multiscale method [18], multiscale finite element method (MsFEM) [17], two-scale finite element methods [22], two-scale conservative subgrid approaches [2,21], and heterogeneous multiscale method (HMM) [14] have been proposed. We remark that special basis functions in finite element methods have been used earlier in [4]. The generalized finite element method has also been introduced in [3] using special basis function. Multiscale finite element methodology has been modified and successfully applied to two-phase flow simulations in [19,20] and later in [8,1]. Arbogast [2] used variational multiscale strategy and constructed a multiscale method for two-phase flow simulations.

In this paper, we propose a multiscale finite element approach in which the basis functions are constructed using the solution of the global fine-scale problem at initial time (only). The heterogeneities of the porous media are typically well represented in the global fine-scale solutions. In particular, the connectivity of the media is properly embedded into the global fine-scale solution. Thus, for the porous media with channelized features (where the high/low permeability region has long-range connectivity), this type of approach is expected to work better. Indeed, our computations show that our modified approach performs better, for porous media with channelized structure, than the approaches in which the basis functions are constructed using only local information. We present some analysis to justify our numerical observations. For the analysis, we use a pressure-streamline coordinate system at initial time for a simplified channelized media. In this coordinate system, one can perform asymptotic expansion and show that the variations of leading order pressure across streamlines are negligible, and the pressure depends smoothly on the pressure at the initial time. Furthermore, we show that global basis functions can represent the leading order pressure accurately.

In our numerical simulations, we have used cross-sections of recent benchmark permeability fields, such as the SPE comparative solution project [10], in which the porous media have a channelized structure and a large aspect ratio. We would like to remark that our proposed approach is different from the oversampling method for multiscale finite element methods [18]. In particular, we use only the global solution of the fine-scale problem at an initial time to extract boundary conditions for the basis functions. On the other hand, the oversampling technique uses the solutions of the larger problems to construct the basis functions directly. Moreover, the proposed multiscale finite element solution is accurate at the initial time. Finally, we would like to note that the global solutions in upscaling procedures have been previously used in [7], which motivated our work. The authors in [7] show that the upscaled models that use the local information tend to perform worse for channelized porous media. Global information within mixed multiscale finite element methods was first used in [1]. In this paper, we perform numerical tests where the global flow direction has changed. We have also tested various ranges of mobility and observed very good agreement when modified basis functions are used. Finally, we have used modified basis functions for certain linear and nonlinear parabolic equations. We have observed an order of magnitude of improvement in the error for permeability fields from the SPE comparative solution project.

This paper is organized in the following way. In the next section we present the details of modified multiscale finite element methods. The numerical results are presented in section three. In Appendix A, we present some theoretical results related to the modified multiscale finite element method.

2. Modified multiscale finite element methods

We consider two-phase flow in a reservoir Ω under the assumption that the displacement is dominated by viscous effects; i.e. we neglect the effects of gravity, compressibility, and capillary pressure. Porosity will be considered to be constant. The two phases will be referred to as water and oil, designated by subscripts w and o, respectively. We write Darcy's law, with all quantities dimensionless, for each phase as follows:

$$v_{\mathrm{j}} = -\frac{k_{\mathrm{rj}}(S)}{\mu_{\mathrm{j}}} k \cdot \nabla p, \tag{2.1}$$

where v_j is the phase velocity, k is the permeability tensor, k_{rj} is the relative permeability to phase j (j = o, w), S is the water saturation (volume fraction), p is pressure and μ_j is the viscosity of phase j (j = o, w). In this work, a single set of relative permeability curves is used and k is assumed to be a diagonal tensor. Combining Darcy's law with a statement of conservation of mass allows us to express the governing equations in terms of the so-called pressure and saturation equations:

$$\nabla \cdot (\lambda(S)k \cdot \nabla p) = q, \tag{2.2}$$

$$\frac{\partial S}{\partial t} + v \cdot \nabla f(S) = 0, \tag{2.3}$$

where λ is the total mobility, f is the fractional flow of water, q is a source term and v is the total velocity, which are respectively given by:

$$\lambda(S) = \frac{k_{rw}(S)}{\mu_w} + \frac{k_{ro}(S)}{\mu_o}, \quad f(S) = \frac{k_{rw}(S)/\mu_w}{k_{rw}(S)/\mu_w + k_{ro}(S)/\mu_o}, \tag{2.4}$$

$$v = v_w + v_o = -\lambda(S)k \cdot \nabla p. \tag{2.5}$$

The above descriptions are referred to as the fine model of the two-phase flow problem. Typical boundary conditions for (2.2) considered in this paper are fixed pressure at some portions of the boundary and no-flow on the rest of the boundary. For the saturation Eq. (2.3), we impose $S = 1$ on the inflow boundaries. For simplicity, in further analysis we will assume $q = 0$.

The upscaling of two-phase flow systems is discussed by many authors [9,5,13]. In most upscaling procedures, the coarse-scale pressure equation is of the same form as the fine-scale Eq. (2.2), but with an equivalent grid block permeability tensor k^* replacing k. For a given coarse-scale grid block, the tensor k^* is generally computed through the solution of the pressure equation over the local fine-scale region corresponding to the particular coarse block [12]. Coarse-grid k^* computed in this manner has been shown to provide accurate solutions to the coarse-grid pressure equation. As we mentioned in Section 1, for channelized porous media, the global information can be used in calculation of effective coarse-grid permeability [7], but these upscaling approaches are not exact at the initial time.

The objective of this work is to propose an accurate multiscale method. We will use the multiscale finite element framework, though a finite volume element method is chosen as a global solver. Finite volume method is chosen because, by its construction, it satisfies the numerical local conservation which is important in groundwater and reservoir simulations. Let $\mathscr{K}^h$ denote the collection of coarse elements/rectangles K. Consider a coarse element K, and let ξ_K be its center. The element K is divided into four rectangles of equal area by connecting ξ_K to the midpoints of the element's edges. We denote these quadrilaterals by K_ξ, where $\xi \in Z_h(K)$, are the vertices of K. Also, we denote $Z_h = \cup_K Z_h(K)$ and $Z_h^0 \subset Z_h$ the vertices which do not lie on the Dirichlet boundary of Ω. The control volume V_ξ is defined as the union of the quadrilaterals K_ξ sharing the vertex ξ.

The key idea of the method is the construction of basis functions on the coarse grids, such that these basis functions capture the small-scale information on each of these coarse grids. The method that we use follows its finite element counterpart presented in [18]. The basis functions are constructed from the solution of the leading order homogeneous elliptic equation on each coarse element with some specified boundary conditions. Thus, if we consider a coarse element K that has d vertices, the local basis functions ϕ_i, $i = 1, \ldots, d$ are set to satisfy the following elliptic problem:

$$\begin{aligned} &-\nabla \cdot (k \cdot \nabla \phi_i) = 0 \quad \text{in } K, \\ &\phi_i = g_i \quad \text{on } \partial K, \end{aligned} \tag{2.6}$$

for some function g_i defined on the boundary of the coarse element (or representative volume element, RVE) K. Hou et al. [18] have demonstrated that a careful choice of boundary conditions would improve the accuracy of the method. In previous findings, the function g_i for each i is chosen to vary linearly along ∂K or to be the solution of the local one-dimensional problems [19] or the solution of the problem in a slightly larger domain is chosen to define the boundary conditions. The boundary conditions for the basis functions that are used in this paper will be discussed later. We will require $\phi_i(x_j) = \delta_{ij}$. Finally, a nodal basis function associated with the vertex x_i in the domain Ω is constructed from the combination of the local basis functions that share this x_i

and zero elsewhere. We would like to note that one can use an approximate solution of (2.6) when it is possible. For example, in the case of periodic or scale separation cases, the basis functions can be approximated using homogenization expansion (see [15]). This type of simplification is not applicable for problems considered in this paper.

Next, we denote by V^h the space of our approximate pressure solution, which is spanned by the basis functions $\{\phi_j\}_{x_j \in Z_h^0}$. Then we formulate the finite dimensional problem corresponding to finite volume element formulation of (2.2). A statement of mass conservation on a coarse control volume V_x is formed from (2.2), where now the approximate solution is written as a linear combination of the basis functions. Assembly of this conservation statement for all control volumes would give the corresponding linear system of equations that can be solved accordingly. The resulting linear system has incorporated the fine-scale information through the involvement of the nodal basis functions on the approximate solution. To be specific, the problem now is to seek $p^h \in V^h$ with $p^h = \sum_{x_j \in Z_h^0} p_j \phi_j$ such that

$$\int_{\partial V_\xi} \lambda(S) k \cdot \nabla p^h \cdot n \, \mathrm{d}l = 0, \tag{2.7}$$

for every control volume $V_\xi \subset \Omega$. Here $\vec{n}$ defines the normal vector on the boundary of the control volume, ∂V_ξ and S is the fine-scale saturation field at this point. We note that concerning the basis functions, a vertex-centered finite volume difference is used to solve (2.6), and using the harmonic average to approximate the permeability k at the edges of fine control volumes.

The main idea of the modified multiscale finite volume element method (MsFVEM) is to use the solution of the fine-scale problem at time zero to determine the boundary conditions for the basis functions. The basis functions are constructed using these boundary conditions. To describe the method, we denote the solution of (2.2) at time zero by $p^{\text{init}}(x)$. For simplicity, we will assume $S = 0$ at time zero. In defining $p^{\text{init}}(x)$, we use the actual boundary conditions of the global problem. $p^{\text{init}}(x)$ depends on global boundary conditions, and, generally, is updated each time when global boundary conditions change. For some special cases, one does not necessarily need to update p^{init} when boundary conditions change. We will discuss it later. The boundary conditions in (2.6) for modified basis functions are defined in the following way. For each rectangular element K with vertices x_i ($i = 1, 2, 3, 4$) denote by $\phi_i(x)$ a restriction of the nodal basis on K, such that $\phi_i(x_j) = \delta_{ij}$. At the edges where $\phi_i(x) = 0$ at both vertices, we take boundary condition for $\phi_i(x)$ to be zero. Consequently, the basis functions are localized. We only need to determine the boundary condition at two edges which have the common vertex x_i ($\phi_i(x_i) = 1$). Denote these two edges by $[x_{i-1}, x_i]$ and $[x_i, x_{i+1}]$ (see Fig. 2.1). We only need to describe the boundary condition, g_i, for the basis function ϕ_i, along the edges $[x_i, x_{i+1}]$ and $[x_i, x_{i-1}]$. If $p^{\text{init}}(x_i) \neq p^{\text{init}}(x_{i+1})$, then

$$g_i(x)|_{[x_i, x_{i+1}]} = \frac{p^{\text{init}}(x) - p^{\text{init}}(x_{i+1})}{p^{\text{init}}(x_i) - p^{\text{init}}(x_{i+1})}, \quad g_i(x)|_{[x_i, x_{i-1}]} = \frac{p^{\text{init}}(x) - p^{\text{init}}(x_{i-1})}{p^{\text{init}}(x_i) - p^{\text{init}}(x_{i-1})}.$$

If $p^{\text{init}}(x_i) = p^{\text{init}}(x_{i+1}) \neq 0$ then

$$g_i|_{[x_i, x_{i+1}]} = \phi_i^0(x) + \frac{1}{2p^{\text{init}}(x_i)} (p^{\text{init}}(x) - p^{\text{init}}(x_{i+1})),$$

where $\phi_i^0(x)$ is a linear function on $[x_i, x_{i+1}]$ such that $\phi_i^0(x_i) = 1$ and $\phi_i^0(x_{i+1}) = 0$. Similarly,

$$g_{i+1}|_{[x_i, x_{i+1}]} = \phi_{i+1}^0(x) + \frac{1}{2p^{\text{init}}(x_{i+1})} (p^{\text{init}}(x) - p^{\text{init}}(x_{i+1})), \tag{2.8}$$

where $\phi_{i+1}^0(x)$ is a linear function on $[x_i, x_{i+1}]$ such that $\phi_{i+1}^0(x_{i+1}) = 1$ and $\phi_{i+1}^0(x_i) = 0$. If $p^{\text{init}}(x_i) = p^{\text{init}}(x_{i+1}) \neq 0$, then one can also use simply linear boundary conditions. If $p^{\text{init}}(x_i) = p^{\text{init}}(x_{i+1}) = 0$ then linear boundary conditions are used. In the applications considered in this paper, the initial pressure is always positive. Finally, the basis function ϕ_i is constructed by solving (2.6). The choice of the boundary conditions for the basis functions is motivated by the analysis. In particular, we would like to recover the exact fine-scale solution along each edge if the nodal values of the pressure are equal to the values of exact fine-scale pressure. This is the underlying idea for the choice of boundary conditions. Using this property and Cea's lemma one can show that the pressure obtained from the numerical solution is equal to the underlying fine-scale pressure.

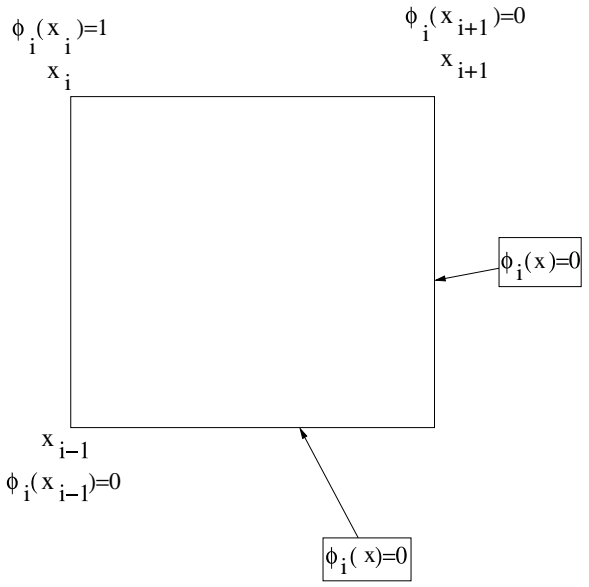

Fig. 2.1. Schematic description of nodal points.

First, we would like to note that these basis functions are local. We only use the global solution, p^{init}, to construct the boundary conditions of the local multiscale bases. The local multiscale bases cannot be constructed directly from the global solution, p^{init}. It can be easily shown that these basis functions are linearly independent, and thus form a basis. Moreover, the sum of these basis functions is equal to 1 in each coarse element, except in the elements where $p^{\text{init}}(x_i) = p^{\text{init}}(x_{i+1}) \neq 0$. Indeed, it can be directly verified that $\sum_{i=1}^{4} \phi_i(x) = 1$ on the boundary. Because $\sum_{i=1}^{4} \phi_i(x)$ satisfies the linear elliptic equation within an element K, it follows that $\sum_{i=1}^{4} \phi_i(x) = 1$ in each coarse element K. One can easily modify one of the basis functions in elements with $p^{\text{init}}(x_i) = p^{\text{init}}(x_{i+1}) \neq 0$ to guarantee their sum is equal to one. For example, changing g_{i+1} (see (2.8)) to $g_{i+1}|_{[x_i,x_{i+1}]} = \phi^0_{i+1}(x) - \frac{1}{2p^{\text{init}}(x_{i+1})}(p^{\text{init}}(x) - p^{\text{init}}(x_{i+1}))$ will guarantee that their sum is equal to one. However, as we will show next, with this modification the multiscale finite element solution is not exact at time zero, which is important in our applications.

Next, we show that if these basis functions are used for linear elliptic equations (with $\lambda(S) = 1$), then the resulting multiscale finite element solution is exact. We will show this for the multiscale finite element method. In the multiscale finite element method, the coarse-scale formulation (2.7) is given by

$$\sum_i p_i \int_\Omega \lambda(S) k \nabla \phi_i \cdot \nabla \phi_j \, \mathrm{d}x = 0,$$

where p_i are nodal pressure values on the coarse-grid. From the stability of multiscale finite element methods (see [16]), we have

$$\|p - p^h\| \leqslant C \inf_{q^h} \|p - q^h\|,$$

where $q^h = \sum q_i \phi_i$. Choosing the nodal values of q_i equal to the value of the fine-scale solution, one can easily show that q^h is equal to the fine-scale solution on the boundary of coarse blocks. This can be verified by direct computation. If $p^{\text{init}}(x_i) \neq p^{\text{init}}(x_{i+1})$, then on $[x_i, x_{i+1}]$ we have

$$\begin{aligned} &p^{\text{init}}(x_i) g_i(x)|_{[x_i,x_{i+1}]} + p^{\text{init}}(x_{i+1}) g_{i+1}(x)|_{[x_i,x_{i+1}]} \\ &\quad = p^{\text{init}}(x_i) \frac{p^{\text{init}}(x) - p^{\text{init}}(x_{i+1})}{p^{\text{init}}(x_i) - p^{\text{init}}(x_{i+1})} + p^{\text{init}}(x_{i+1}) \frac{p^{\text{init}}(x) - p^{\text{init}}(x_i)}{p^{\text{init}}(x_{i+1}) - p^{\text{init}}(x_i)} = p^{\text{init}}(x). \end{aligned} \tag{2.9}$$

If $p^{\text{init}}(x_i) = p^{\text{init}}(x_{i+1}) \neq 0$, then on $[x_i, x_{i+1}]$ we have

$$p^{\text{init}}(x_i)g_i(x)|_{[x_i,x_{i+1}]} + p^{\text{init}}(x_{i+1})g_{i+1}(x)|_{[x_i,x_{i+1}]}$$
$$= p^{\text{init}}(x_i)\left[\phi_i^0(x) + \frac{1}{2p^{\text{init}}(x_i)}(p^{\text{init}}(x) - p^{\text{init}}(x_{i+1}))\right] + p^{\text{init}}(x_{i+1})[\phi_{i+1}^0(x)$$
$$+ \frac{1}{2p^{\text{init}}(x_{i+1})}(p^{\text{init}}(x) - p^{\text{init}}(x_{i+1}))] = p^{\text{init}}(x). \tag{2.10}$$

One can show similar equalities for other edges. Furthermore, because q^h satisfies the underlying fine-scale equation in any coarse block and is equal to the underlying fine-scale solution on the boundary, thus it is equal to the fine-scale solution. For finite volume methods, this statement can also be proved assuming the uniqueness of the discrete solution. We omit this proof here. Our numerical results will demonstrate this. As we mentioned earlier, if $p^{\text{init}}(x_i) = p^{\text{init}}(x_{i+1}) \neq 0$, then the basis functions do not sum up to one. To achieve the latter, one can modify the boundary conditions. But in this case, the multiscale solution at the initial time is not exact. For our computations, it is important to recover the exact fine-scale solution at the initial time. We note that even though the sum of the basis functions may not be one, in some coarse blocks where $p^{\text{init}}(x_i) = p^{\text{init}}(x_{i+1}) \neq 0$, the basis functions still span a function that is approximately one. With direct computations, one can show that $\sum_{i=1}^4 \phi_i$ will be equal to $p^{\text{init}}(x)/p^{\text{init}}(x_i)$ on the edge $[x_i, x_{i+1}]$. Thus, it will be equal to 1 at the vertices, though slightly different from one along the edge. We would like to note that in the presence of source terms on the right hand side of (2.2) in order to recover the exact fine-scale solution, the basis functions need to be modified by incorporating the source term into the right hand side of (2.6). In particular, the corresponding right hand side in (2.6) is an original source term divided by the value of the pressure at the node i, $q/p^{\text{init}}(x_i)$.

We would clarify the difference between the proposed approach and the oversampling method for multiscale finite element methods [18]. Note, we use only the global solution of the fine-scale problem at the initial time and our multiscale finite element solution. On the other hand the main idea of the oversampling method is to use the solutions of the larger problems with some a priori boundary conditions. Typically, four independent solutions are constructed with some known boundary conditions. Then using these solutions, the multiscale basis functions are constructed. In the proposed approach, we use the global solution to obtain only boundary conditions for the multiscale basis functions.

For two-phase flow simulations, we will use IMPES formulation (implicit pressure and explicit saturation) for the computations. Each time the pressure equation is solved and the velocity is computed. Then the velocity is used to update the saturation. For a linear problem, our approach has redundancy because it uses the fine-scale solution. Whereas for two-phase flow simulations, the pressure equation is solved many times. With our modified multiscale finite element method, the pressure equation will be solved using the pre-computed multiscale basis functions at the initial time. We would like to note that the permeability field is the only function that induces the small-scale features of the flow. This small-scale information is incorporated into the multiscale basis functions. Moreover, the saturation dynamics is governed by the permeability field and the saturation field is generally smooth except near sharp fronts with locations determined from the heterogeneous permeability field.

Next, we would like to add a comment how to achieve the low computational complexity with multiscale finite element methods when applied to two-phase flow problems. For every saturation field, MsFVEM produces a corresponding velocity field. The multiscale basis functions should therefore be re-computed each time the saturation profile changes. However, it can be shown that if the saturation is smooth within the coarse block, then the basis functions that take into account the saturation variation within the coarse block are approximately the same as the basis functions that neglect the saturation variation in the coarse block. The error made with this approximation is of order coarse mesh size. Because of this, typically in multiscale simulations (e.g., [20]), one updates the basis functions in time near a sharp front. We have observed that there is only a slight improvement if the basis functions are updated near sharp fronts. In the calculations below, the basis functions are not updated. We only update the basis functions if the global boundary conditions are changed. Below, we present a representative numerical result that compares the simulations when the basis functions are updated everywhere with the results when no update of the basis functions is performed.

Using homogenization techniques for periodic media, one can show that the global multiscale finite element method does not contain the resonance errors, typically observed in multiscale finite element methods that use

local basis functions. This result will be presented elsewhere. However, this analysis does not reveal the capability of the modified multiscale finite element method in capturing long-range features of the flow. In the Appendix A, we present some analysis using the pressure-streamline framework that demonstrates that the modified multiscale finite element method is more efficient for porous media flows with long-range interactions than the standard multiscale finite element method. In a channelized medium, the dominant flow is within the channels. Our analysis assumes a single channel. Here, we briefly mention the main findings presented in the Appendix A. Denote the initial stream function (see (A.1) in Appendix A) and pressure by $\eta = \psi(x, t = 0)$ and $\zeta = p(x, t = 0)$ (ζ is also denoted by p^{init} previously). Then the equation for the pressure can be written as

$$\frac{\partial}{\partial \eta}\left(|k|^2 \lambda(S)\frac{\partial p}{\partial \eta}\right) + \frac{\partial}{\partial \zeta}\left(\lambda(S)\frac{\partial p}{\partial \zeta}\right) = 0. \tag{2.11}$$

For simplicity, $S = 0$ at time zero is assumed. We consider a typical boundary condition that gives high flow within the channel, such that the high flow channel will be mapped into a large slab in (η, ζ) coordinate system (see Fig. A.1). If the heterogeneities within the channel in η direction is not strong (e.g. narrow channel in Cartesian coordinates), the saturation within the channel will depend on ζ. In this case, the leading order pressure will depend only on ζ, and it can be shown that

$$p(\eta, \zeta, t) = p_0(\zeta, t) + \text{high order terms},$$

where $p_0(\zeta, t)$ is the dominant pressure. The explanation of higher order terms is presented in the Appendix A. This asymptotic expansion shows that the time-varying pressure strongly and smoothly depends on the initial pressure (i.e. the leading order term in the asymptotic expansion is a function of initial pressure and time only). Because the global basis functions can recover the initial pressure exactly, the modified basis can capture the global pressure more accurately. In the Appendix A, we discuss more extensively the advantages of the modified multiscale basis functions. We would like to note that our goal is to construct a set of basis functions for the flow equation at initial time that can be used to solve the flow equation on the coarse grid at later times. This is a very important for multi-phase flow simulations, because the flow equations are solved many times and solving the flow equations is CPU demanding. By constructing a set of basis functions at initial time, the flow equation is solved on the coarse grid at later times. Note that for $k(x)$ with scale-separation, this question can be answered within homogenization theory. Moreover, one can construct the homogenized coefficients, k^*. Here, we show that for the fields with strong non-local effects, one can construct basis functions and project the solution into the coarse dimensional space.

We would like to note that the analysis presented in the Appendix A is for a single-channel flow, and can be extended to some more complicated flow scenarios. This is only a simplified model that allows us to demonstrate the importance of global information in constructing the basis functions. We would like to note that global basis functions capture small-scale information similar to the standard multiscale basis functions, i.e. in the case of scale separation, the convergence of the modified multiscale finite element methods is similar to that of the standard multiscale finite element method. This can be established using homogenization techniques. It is important to remark that, one does not know, in general, which channels will be active fluid carriers and that the latter depends on global boundary conditions. The modified multiscale basis functions embed these global features as well as global boundary conditions into the basis functions.

3. Numerical results

In this section, we present representative simulation results for flux functions $f(S)$ with viscosity ratio $\mu_o/\mu_w = 5$. We have tested higher viscosity ratios and observed very similar results. In all cases the systems are considered to be one of the layers of the benchmark test, the SPE comparative project [10] (upper Ness layers). These permeability fields are highly heterogeneous, channelized, and difficult to upscale. In Fig. 3.1 we depict the log-permeability for one of the layers. Simulation results are presented for the total flow rate and the oil cut as a function of pore volume injected (PVI). Note that the oil cut is also referred to as the fractional flow of oil. The oil cut (or fractional flow) is defined as the fraction of oil in the produced fluid and is given by q_o/q_t, where $q_t = q_o + q_w$, with q_o and q_w being the flow rates of oil and water at the production edge of the model. In particular, $q_w = \int_{\partial\Omega^{\text{out}}} f(S) v \cdot n \, d\omega$, $q_t = \int_{\partial\Omega^{\text{out}}} v \cdot n \, d\omega$, and $q_o = q_t - q_w$, where $\partial\Omega^{\text{out}}$ is the

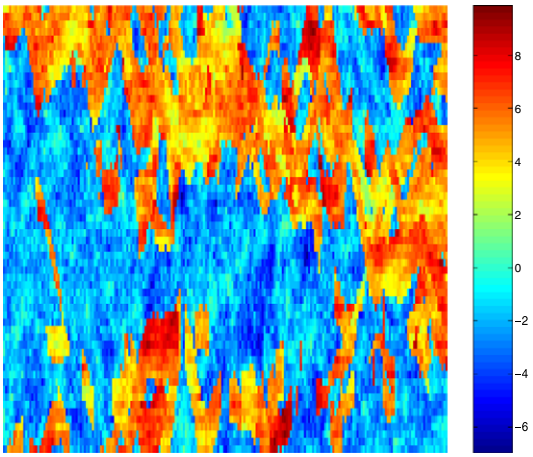

Fig. 3.1. Log-permeability for one of the layers of upper Ness.

outer flow boundary. We will use the notation Q for total flow q_t and F for fractional flow q_o/q_t in numerical results. Pore volume injected, defined as $\mathrm{PVI} = \frac{1}{V_p}\int_0^t q_t(\tau)\,d\tau$, with V_p being the total pore volume of the system, provides the dimensionless time for the displacement. When using multiscale finite element methods for two-phase flow, one can update the basis functions near the sharp fronts. Indeed, sharp fronts modify the local heterogeneities and this can be taken into account by re-solving the local equations, (2.6), for basis functions. If the saturation is smooth in the coarse block, it can be approximated by its average in (2.6), and consequently, the basis functions are not needed to be updated. It can be shown that this approximation yields first-order errors (in terms of coarse mesh size). In our simulations, we have found only a slight improvement if the basis functions are updated, thus the numerical results for the modified MsFVEM presented in this paper do not include the basis function update near the sharp fronts. In all numerical examples, related to the SPE comparative solution project, the fine-scale field is 220×60, while the coarse-scale field is 22×6. We have observed similar results for other coarse grids. We consider two types of boundary conditions. For the first type of boundary conditions, we specify $p = 1$, $S = 1$ along the $x = 0$ edge and $p = 0$ along the $x = 1$ edge. On the rest of the boundaries, we assume no flow boundary condition. We call this type of the boundary condition as side-to-side. The other type of boundary conditions is obtained by specifying $p = 1$, $S = 1$ along the $x = 0$ edge for $0.5 \leqslant z \leqslant 1$ and $p = 0$ along the $x = 1$ edge for $0 \leqslant z \leqslant 0.5$. On the rest of the boundaries, we assume no flow boundary condition. We will be also considering changing boundary conditions, where the boundary conditions are changed from one type to another at certain time.

The objective of our first set of results is demonstrate that the proposed procedure is exact for single phase simulations. In Fig. 3.2, the crossplot between the total flow rate (q_t) for fine-scale solutions and the corresponding multiscale solutions for 50 layers of the upper Ness is plotted. In the left figure the crossplot is depicted for modified MsFVEM and in the right plot it is depicted for the standard MsFVEM. Every point in this figure corresponds to one of the layers of the upper Ness (total 50 layers) of the SPE comparative solution project [10]. The results corresponding to the modified MsFVEM are exact, while there is a deviation in the results of the standard MsFVEM.

Next, we present some representative flow results. In Fig. 3.3, the fractional flow ($F = q_o/q_t$, left figure) and the total flow ($Q = q_t$, right figure) curves are plotted for the layer number 43. One can see clearly that the modified MsFVEM method gives nearly exact results for these integrated responses. The standard MsFVEM tends to overpredict the total flow rate at time zero. This initial error persists at later times, and gives about 15% error at later times for both the total production and fractional flow rates. This phenomena is often observed in upscaling of two-phase flows. In Fig. 3.4, the saturation maps are plotted at $\mathrm{PVI} = 0.5$. This result is representative for saturation profiles at earlier and later times. We can see from these figures that standard MsFVEM (middle figure) tends to miss some of the fine features of the flow. For example, at the lower left corner we observe an overestimation of a small saturation pocket, which does not exist in the fine-scale saturation map (left figure). Moreover, the closer look at the result obtained using the standard MsFVEM shows

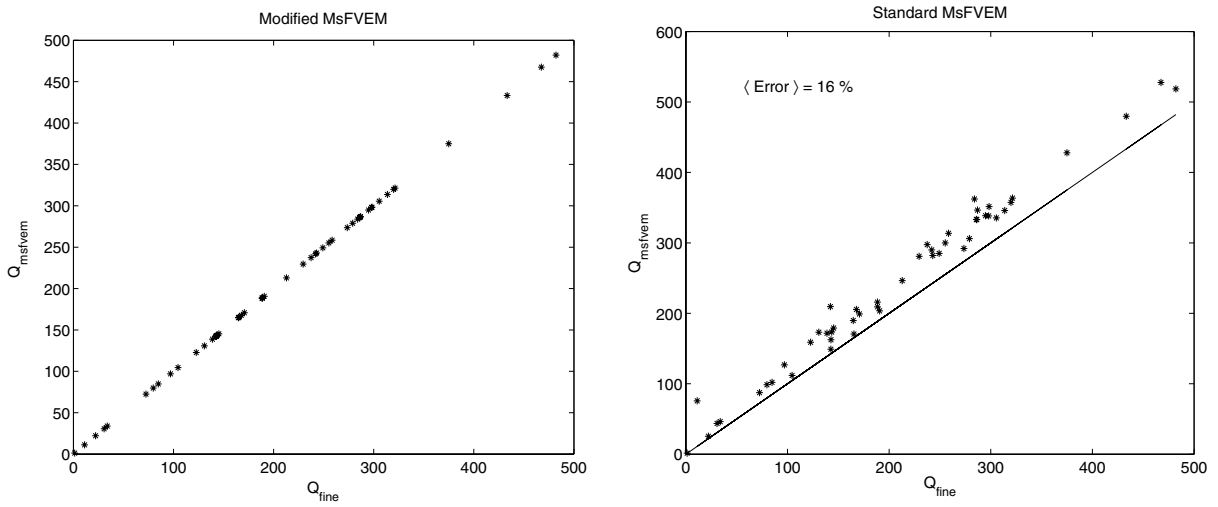

Fig. 3.2. Total flow comparison for 50 layers of upper Ness.

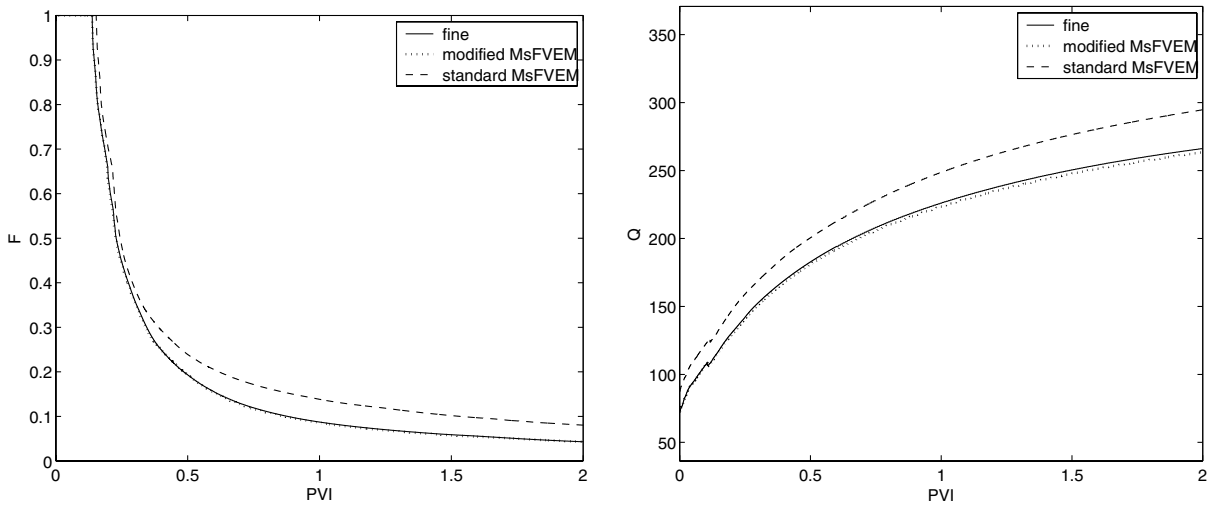

Fig. 3.3. Fractional flow (left figure) and total production (right figure) comparison for standard MsFVEM and modified MsFVEM for side-to-side flow.

that there is an overprediction near the lower boundary of the layer. On the other hand, the result obtained using the modified multiscale finite element method looks exactly the same as the fine-scale solution. The relative L_2 error for the modified MsFVEM is less than 5%, while the relative L_2 error for standard MsFVEM is about 27%. In the next set of results, we repeat these calculations for the corner-to-corner flow. In Fig. 3.5, the fractional flow as well as the production curves are plotted. In Fig. 3.6, the saturation plots are depicted. These results are very similar to the ones obtained with the side-to-side boundary condition.

For the next set of results, we consider another layer of the upper Ness (layer 59). In Fig. 3.7, both fractional flow (left figure) and total flow (right figure) are plotted. We observe that the modified MsFVEM gives almost the exact results for these quantities, while the standard MsFVEM overpredicts the total flow rate, and there are deviations in the fractional flow curve around PVI ≈ 0.6. Note that unlike the previous case, fractional flow for standard MsFVEM is nearly exact at later times (PVI ≈ 2). In Fig. 3.8, the saturation maps are plotted at PVI $= 0.5$. The left figure represents the fine-scale, the middle figure represents the results obtained using standard MsFVEM, and the right figure represents the results obtained using the modified

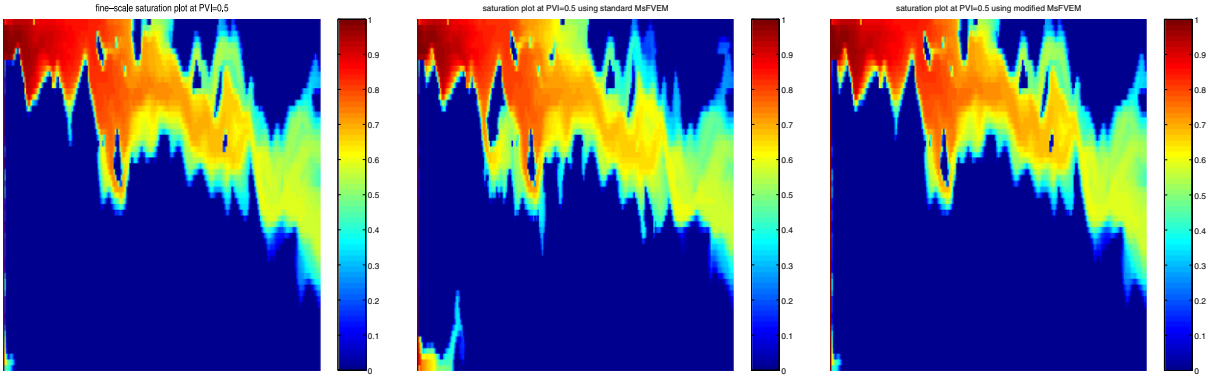

Fig. 3.4. Saturation maps at PVI = 0.5 for fine-scale solution (left figure), standard MsFVEM (middle figure), and modified MsFVEM (right figure). Side-to-side boundary condition is used.

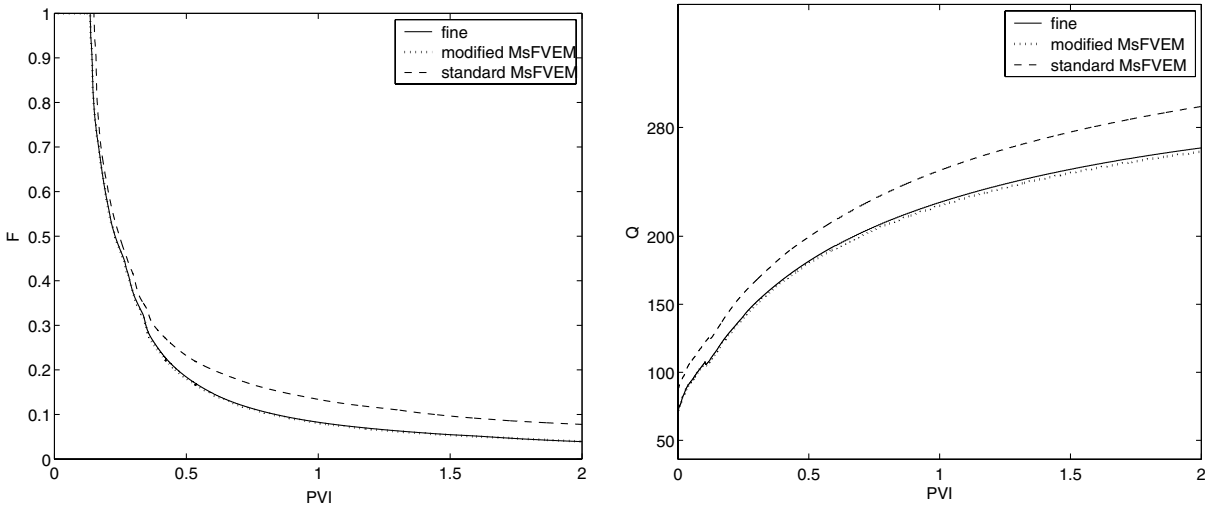

Fig. 3.5. Fractional flow (left figure) and total production (right figure) comparison for standard MsFVEM and modified MsFVEM for corner-to-corner flow.

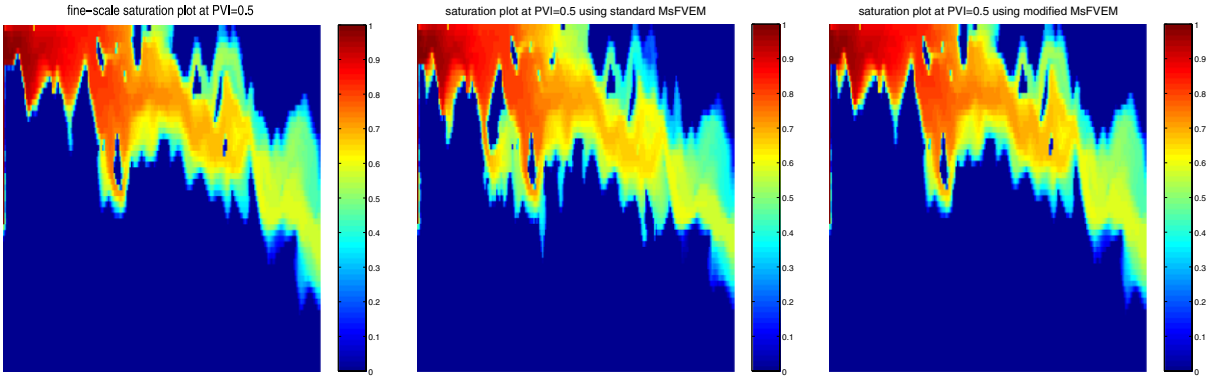

Fig. 3.6. Saturation maps at PVI = 0.5 for fine-scale solution (left figure), standard MsFVEM (middle figure), and modified MsFVEM (right figure). Corner-to-corner boundary condition is used.

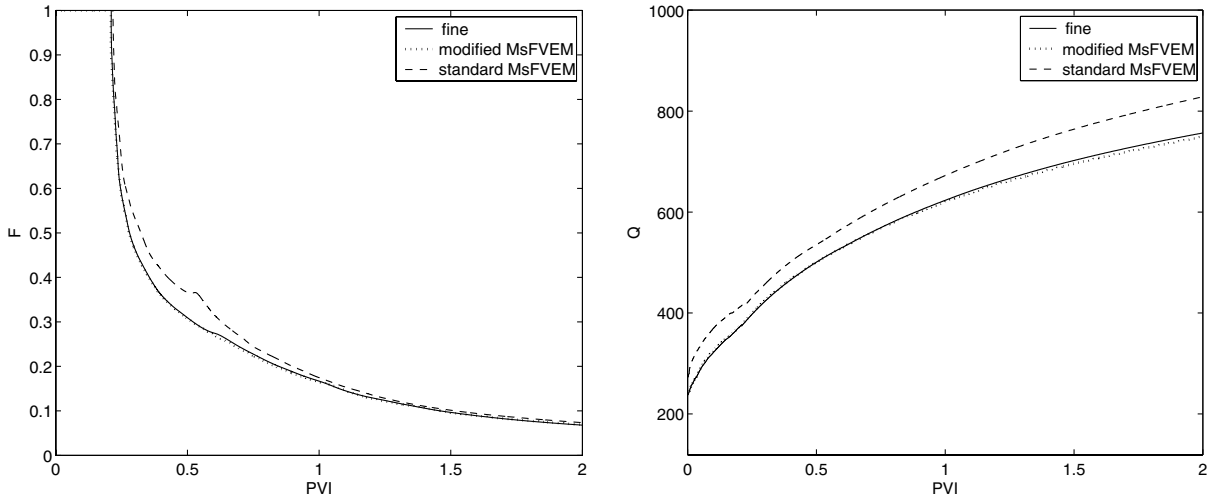

Fig. 3.7. Fractional flow (left figure) and total production (right figure) comparison for standard MsFVEM and modified MsFVEM for corner-to-corner flow.

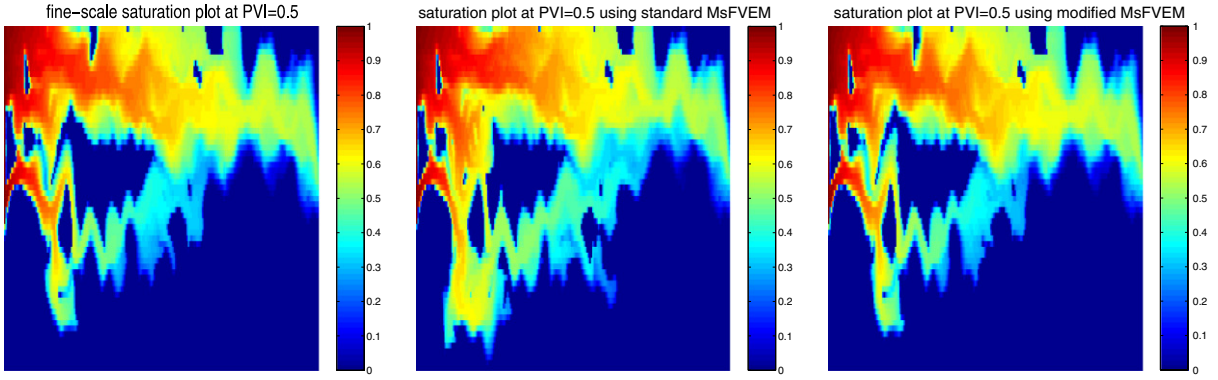

Fig. 3.8. Saturation maps at PVI = 0.5 for fine-scale solution (left figure), standard MsFVEM (middle figure), and modified MsFVEM (right figure). Corner-to-corner boundary condition is used.

MsFVEM. We observe from this figure that the saturation map obtained using standard MsFVEM has some errors. These errors are more evident near the lower left corner. The results of the saturation map obtained using the modified MsFVEM is nearly the same as the fine-scale saturation field. It is evident from these figures that the modified MsFVEM performs better than the standard MsFVEM.

The next case considered involves the same permeability fields, but with changing boundary conditions. The flow is initially from left to right, as specified in the previous example. However, at a time of 0.6 PVI, the global boundary condition is changed such that the flow is driven from the lower left corner of the model to the upper right corner. This is achieved by specifying $p = 1$, $S = 1$ along the $x = 0$ edge for $0 \leqslant z \leqslant 0.5$ and $p = 0$ along the $x = 1$ edge for $0.5 \leqslant z \leqslant 1$ for $t > 0.6$ PVI. At the time when the boundary condition is changed, we update the global basis functions by using the fine-grid pressure at 0.6 PVI, and further calculations are performed using the updated basis functions. Simulation results for layer 43 are shown in Fig. 3.9. Note that at PVI = 0.6, one can observe a discontinuity (“kink”) in the fractional flow curve. This is caused by the change in boundary conditions. In Fig. 3.10, we plot saturation profiles after boundary conditions are changed, at 0.7 PVI. The multiscale simulations using the global basis functions again track the fine-grid solution much more closely than standard multiscale method with local basis functions. In Fig. 3.11, the boundary conditions at 0.6 PVI are changed to $p = 1$, $S = 1$ along the $x = 0$ edge for $0.5 \leqslant z \leqslant 1$, $p = 0$ along the $x = 1$ edge for $0 \leqslant z \leqslant 0.5$, and no flow on the rest of the boundary, i.e. the flow direction has changed from top corner

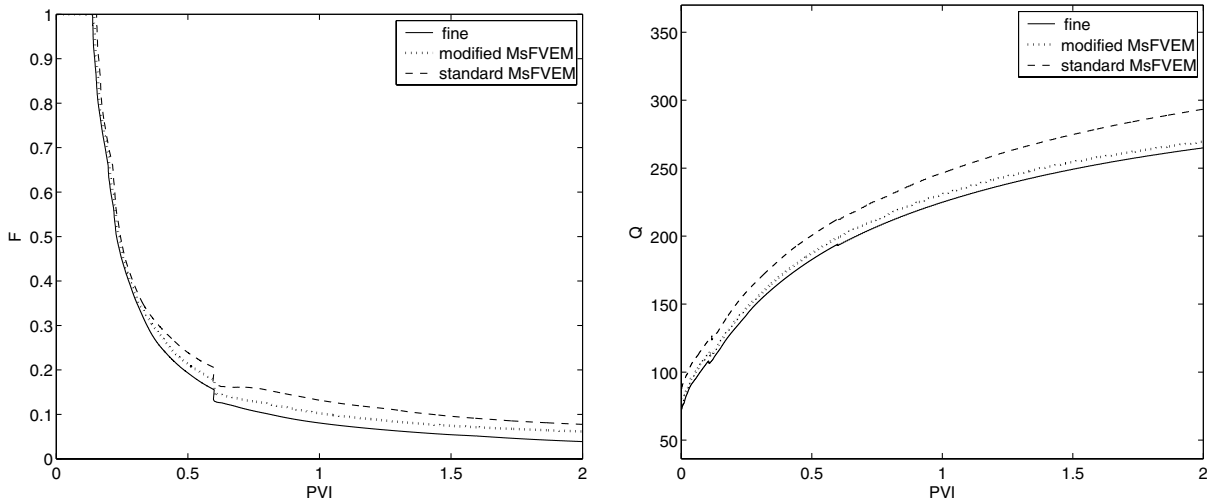

Fig. 3.9. Fractional flow (left figure) and total production (right figure) comparison for standard MsFVEM and modified MsFVEM for changing boundary conditions.

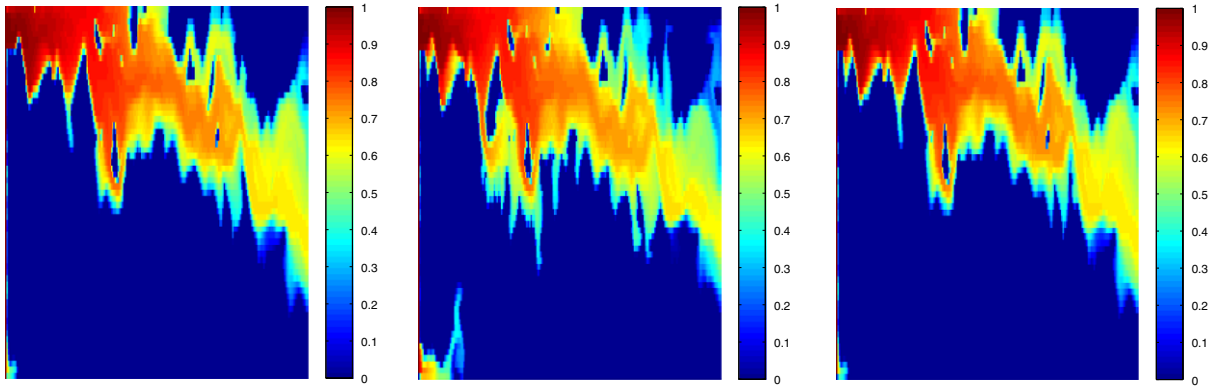

Fig. 3.10. Saturation maps at PVI = 0.5 for fine-scale solution (left figure), standard MsFVEM (middle figure), and modified MsFVEM (right figure). Changing boundary condition is used.

to bottom corner. We found this to be one of the extreme cases, where the total flow rate drops significantly. In this case, the standard multiscale finite element method has large errors near 0.6 PVI, while we see from Fig. 3.11 that modified multiscale method performs very well. Again, we see an improvement when global basis functions are used in the simulations. In Figs. 3.12 and 3.13, the same test is performed for the layer 50. Again, we see an improvement rendered by the modified multiscale finite element method.

In our next set of numerical results, we compare modified MsFVEM and standard MsFVEM where the basis functions are updated everywhere at each time step. The objective of these numerical results is to show that the update of basis functions does not give significant improvement. We only present fractional flow and production curves. For saturation plots, we have also observed almost no improvement when basis functions are updated. In Figs. 3.14 and 3.15, the fractional flow and total production curves for layers 67 and 68 are plotted. We observed from this figure that the improvement achieved by updating the basis functions is insignificant. We have tested many of the layers and observed almost no improvement when the basis functions are updated everywhere.

Our final numerical results are for the permeability fields that are generated using two-point statistics. In general, it is easier to handle these types of heterogeneities using upscaling or multiscale methods. To generate this permeability field, we have used GSLIB algorithm [11]. The permeability is log-normally distributed with

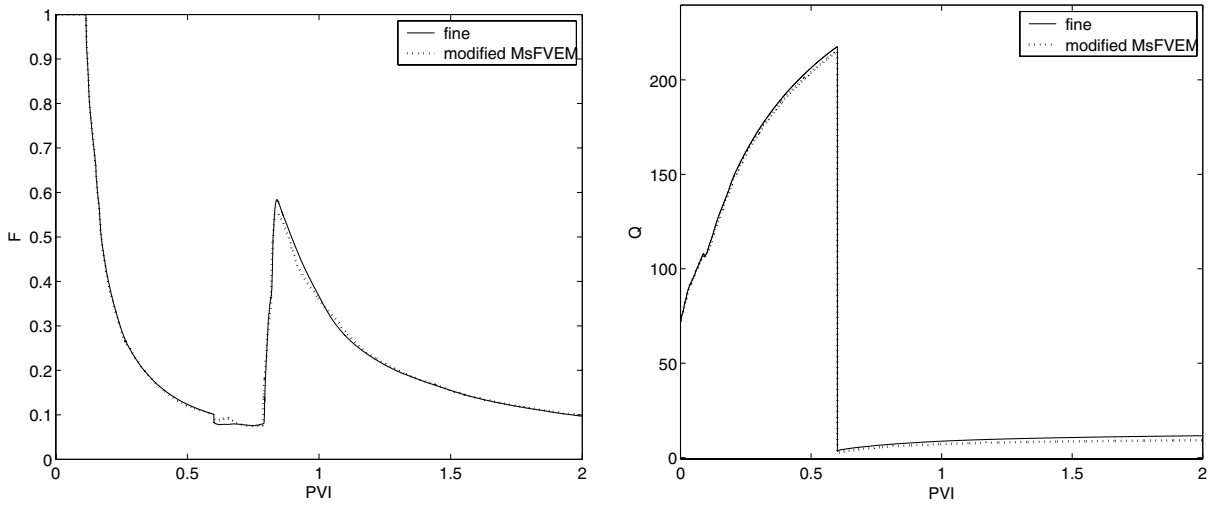

Fig. 3.11. Fractional flow (left figure) and total production (right figure) comparison for standard MsFVEM and modified MsFVEM for changing boundary conditions.

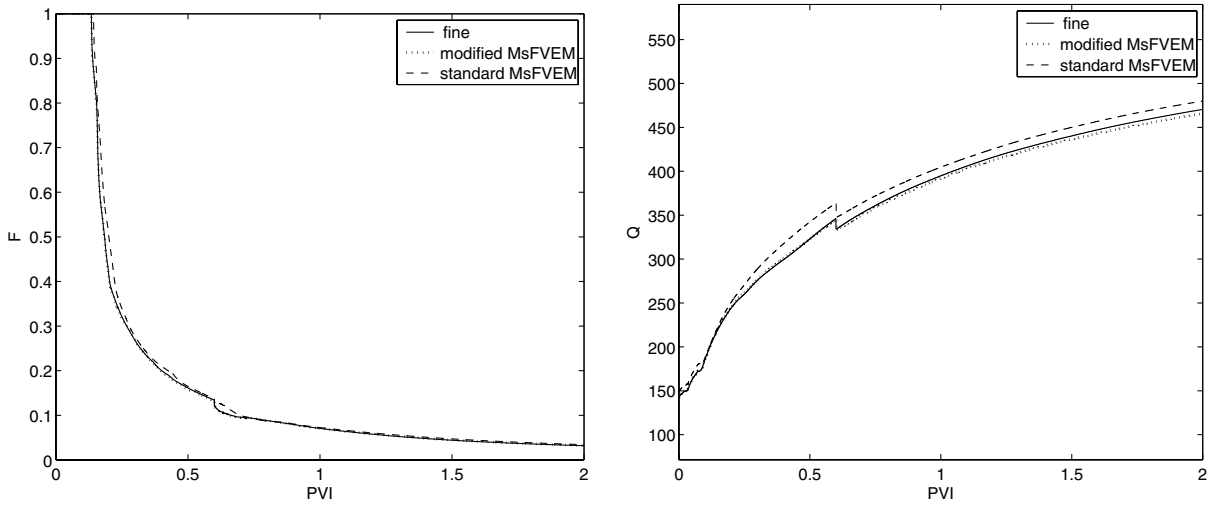

Fig. 3.12. Fractional flow (left figure) and total production (right figure) comparison for standard MsFVEM and modified MsFVEM for changing boundary conditions.

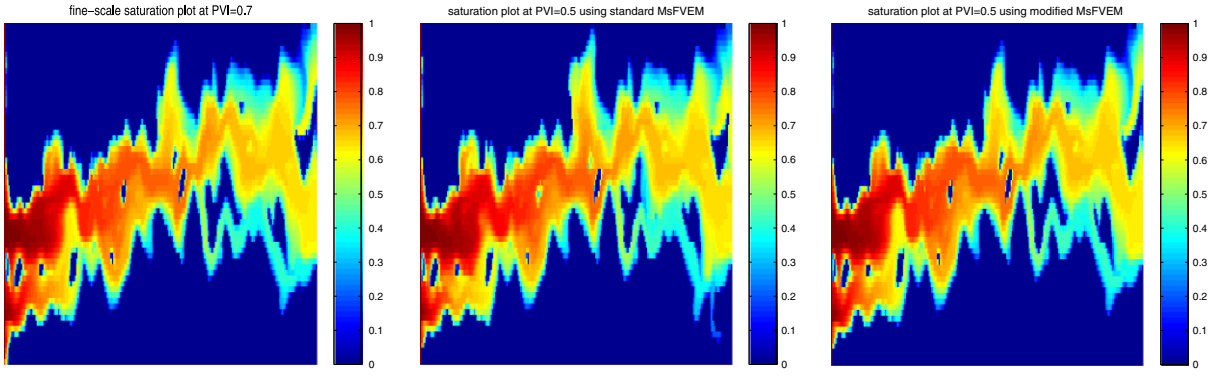

Fig. 3.13. Saturation maps at PVI = 0.5 for fine-scale solution (left figure), standard MsFVEM (middle figure), and modified MsFVEM (right figure). Changing boundary condition is used.

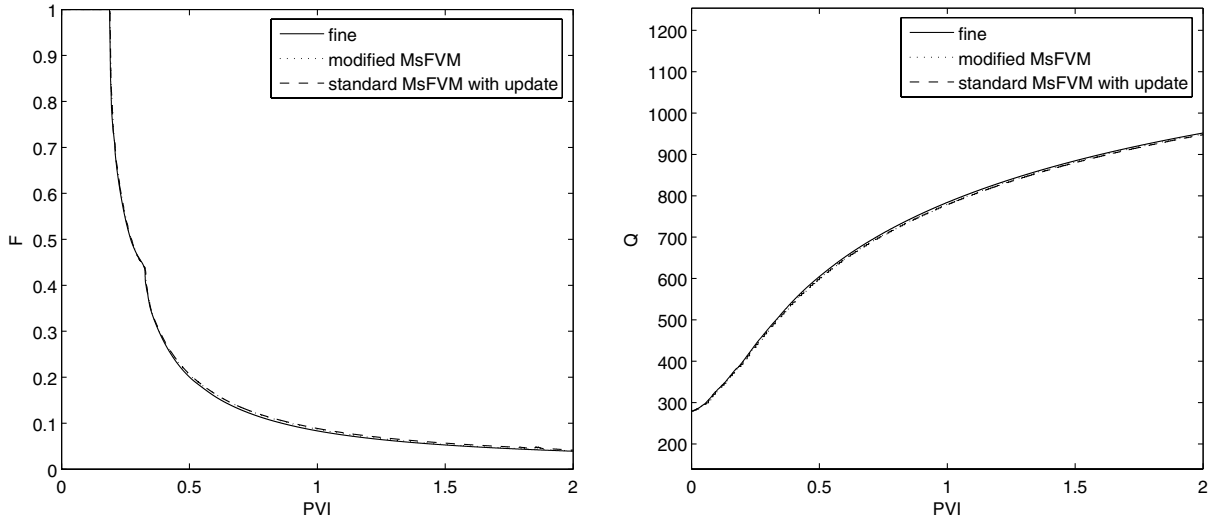

Fig. 3.14. Fractional flow (left figure) and total production (right figure) comparison for standard MsFVEM when the basis functions are updated everywhere and modified MsFVEM for layer 67.

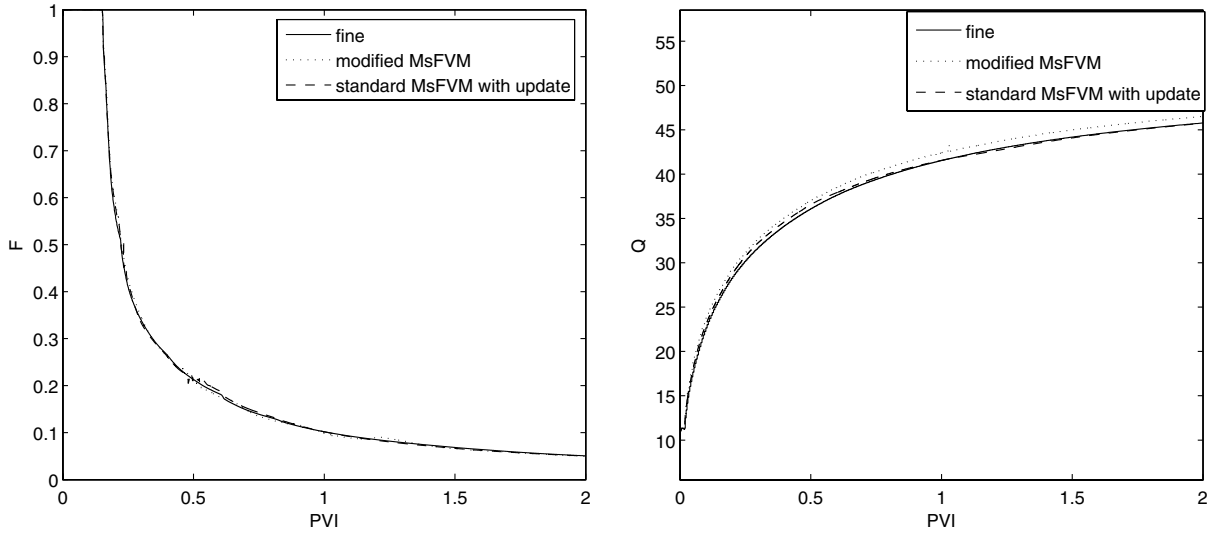

Fig. 3.15. Fractional flow (left figure) and total production (right figure) comparison for standard MsFVEM when the basis functions are updated everywhere and modified MsFVEM for layer 68.

prescribed variance $\sigma^2 = 1.5$ (σ^2 here refers to the variance of $\log k$) and some correlation structure. The correlation structure is specified in terms of dimensionless correlation lengths in the x and z-directions, $l_x = 0.4$ and $l_z = 0.04$, nondimensionalized by the system length. Spherical variogram is used [11]. In this numerical example, the fine-scale field is 120×120, while the coarse-scale field is 12×12. In Fig. 3.16, we plot the fractional flow (left figure) as well as the total production (right figure). One can see the improvement obtained using the modified MsFVEM, though standard MsFVEM also performs very well. For saturation plots, we observed smaller L_2 relative errors. In particular, the standard MsFVEM gives nearly 7% errors, while the modified MsFVEM gives less than 3% errors. Our analysis presented in the Appendix A explains why the standard multiscale finite element method work better for permeability fields generated using two-point geostatistics, where layering is parallel to Cartesian grid (see Fig. 3.17).

Finally, we would like to note that we have applied the modified multiscale finite element methods to certain linear and nonlinear parabolic equations, where channelized permeability fields are used. We have

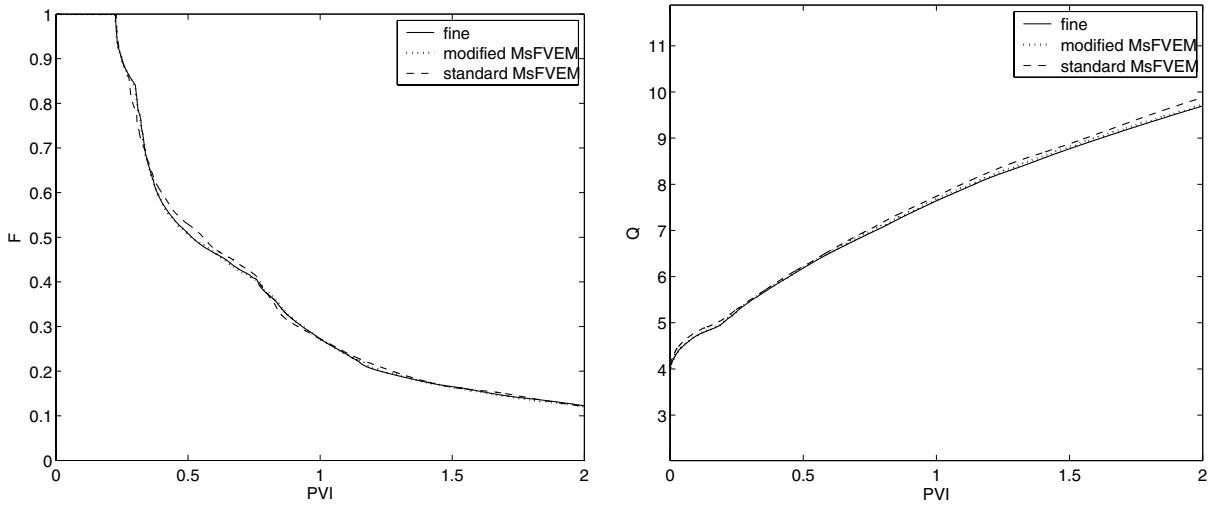

Fig. 3.16. Fractional flow (left figure) and total production (right figure) comparison for standard MsFVEM and modified MsFVEM for corner-to-corner flow.

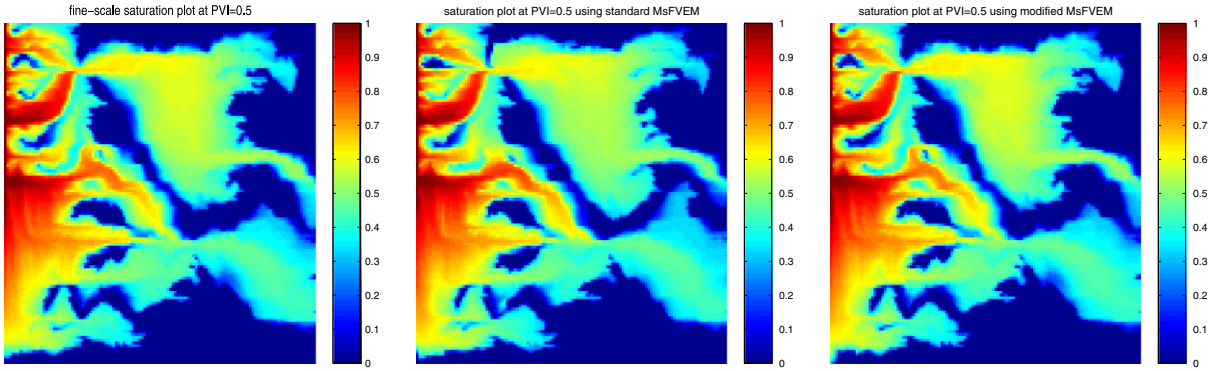

Fig. 3.17. Saturation maps at PVI = 0.5 for fine-scale solution (left figure), standard MsFVEM (middle figure), and modified MsFVEM (right figure). Corner-to-corner boundary condition is used.

observed an order of magnitude improvement when using the modified multiscale finite element methods. For example, for linear parabolic equations, the relative L_2 error for standard multiscale finite element is about 3%, while for the modified multiscale finite element method we have observed a 0.4% error. Similarly, for nonlinear flows, such as Richards equation, we have observed an order of magnitude improvement in the relative errors. We would like also to note that the modified MsFVEM can be extended to 3-D.

4. Concluding remarks

In this paper we propose a modified multiscale finite element method for two-phase flow simulations using the global fine-scale solution of single-phase equations. The main goal of this paper is to better capture the long-range features that occur in two-phase flow simulations. For this purpose, we choose permeability fields from the SPE comparative solution project [10], which have the channelized structure. We demonstrate numerically that the proposed method is capable of capturing the long-range flow features accurately for these fields. On the other hand, for more regular fields generated using two-point statistics, the standard MsFVEM works as well as the modified MsFVEM, though there is some slight improvement. We present some analysis that allows us to explain why the modified multiscale finite element method captures the global information better. We would like to note that the modified basis functions depend on global boundary conditions and need to be modified if the global boundary conditions are changed. Consequently, they are more applicable

for problems where global boundary conditions do not change frequently. Finally, we have observed an order of magnitude improvement if the global basis functions are used for some linear and nonlinear parabolic equations in heterogeneous media, where the heterogeneities have channelized structure.

Acknowledgments

Efendiev acknowledges Louis Durlofsky, Patrick Jenny, and Xiao-Hui Wu for many useful discussions and suggestions. The research of Y.E. is partially supported by NSF Grants DMS-0327713 and EIA-0218229 and DOE Grant DE-FG02-05ER25669. The research of T.Y.H. is partially supported by the NSF ITR Grant ACI-0204932.

Appendix A. Capturing non-local effects with global basis functions

In this appendix, we present some analysis for the modified multiscale finite element methods for channelized porous media. For the analysis, we will use streamline-pressure coordinates. We will show that the modified multiscale finite element method captures the non-local effects induced by high flow channels. To show this, we present some asymptotic results. These results basically show that time-varying pressure is strongly influenced by the initial pressure field. Then we show that the modified multiscale methods can capture non-local effects more efficiently, because long-range information along these channels is accurately incorporated into the modified basis functions.

We will restrict our analysis to a two-dimensional case and assume the heterogeneous porous media are isotropic, $k(x) = k(x)I$. The stream function is defined as $\nabla \times \psi = v = (v_1, v_2)$. Note that the stream function ψ is a scalar field in 2-D defined by

$$\partial\psi/\partial x_1 = -v_2, \quad \partial\psi/\partial x_2 = v_1. \tag{A.1}$$

Using incompressibility, one can easily show that

$$\nabla \cdot \left(\frac{1}{\lambda(S)k} \nabla\psi \right) = 0.$$

We will assume that the boundary conditions are prescribed by no flow on the lateral sides and $p = 1$ on the left vertical edge and $p = 0$ on the right vertical edge, and initially $S = 0$ inside the domain and $S = 1$ at the left vertical edge. The boundary conditions on the stream function depend on the pressure and velocity field. For our specified boundary conditions, the stream function will be constant on lateral edges. Because stream function is defined up to a constant, we can define it by zero at the bottom edge. The value at the top edge is determined by the total flow rate. It can be easily shown that

$$\nabla\psi \cdot \nabla p = -k \frac{\partial p}{\partial x_2} \frac{\partial p}{\partial x_1} + k \frac{\partial p}{\partial x_2} \frac{\partial p}{\partial x_1} = 0.$$

Consequently, (ψ,p) define an orthogonal curvilinear system of coordinates. Because of the orthogonality of the coordinate system, the associated Euclidean metric tensor, g is diagonal and

$$g_{11} = |\nabla p|^2, \quad g_{22} = |\nabla\psi|^2. \tag{A.2}$$

It can be easily shown that in the streamline-pressure coordinate system the elliptic equation becomes:

$$\begin{aligned} \nabla \cdot (k\nabla z) &= \sqrt{det(g)} \left(\frac{\partial}{\partial\psi} \left(\frac{|\nabla\psi|^2}{|\nabla p|^2} \frac{\partial z}{\partial\psi} \right) + \frac{\partial^2 z}{\partial p^2} \right), \\ \nabla \cdot \left(\frac{1}{k} \nabla z \right) &= \sqrt{det(g)} \left(\frac{\partial^2 z}{\partial\psi^2} + \frac{\partial}{\partial p} \left(\frac{|\nabla p|^2}{|\nabla\psi|^2} \frac{\partial z}{\partial p} \right) \right). \end{aligned} \tag{A.3}$$

Furthermore, it can be easily verified that

$$k = \frac{|\nabla\psi|}{|\nabla p|}. \tag{A.4}$$

To understand how the multiscale finite element method captures the non-local effects, we will assume that there is a high permeability channel in the porous media. Moreover, we assume that the flow along the channel is a dominant flow (i.e. we neglect the cross flow due to the mobility). This assumption holds if the permeability $\lambda(S)k$ is much larger in the channel compared to the permeability outside the channel. We would like to note that although this assumption can be considered a good approximation for the problems with adverse mobility ratio and high flow channels of permeability, here we use it to show that our proposed approach can capture the non-local effects induced by the high permeability channels efficiently. Denote the initial stream function and pressure by $\eta = \psi(x, t = 0)$ and $\zeta = p(x, t = 0)$. For simplicity, we will assume $S = 0$ at time zero. Then the equation for pressure and stream function can be written down in this curvilinear orthogonal coordinate system using (A.2), (A.4), and (A.3)

$$\begin{aligned} &\frac{\partial}{\partial\eta}\left(|k|^2\lambda(S)\frac{\partial p}{\partial\eta}\right) + \frac{\partial}{\partial\zeta}\left(\lambda(S)\frac{\partial p}{\partial\zeta}\right) = 0,\\ &\frac{\partial}{\partial\eta}\left(\frac{1}{\lambda(S)}\frac{\partial\psi}{\partial\eta}\right) + \frac{\partial}{\partial\zeta}\left(\frac{1}{\lambda(S)|k|^2}\frac{\partial\psi}{\partial\zeta}\right) = 0. \end{aligned} \tag{A.5}$$

Applying the same change of variables to saturation equation, we get

$$\frac{\partial S}{\partial t} + (v\cdot\nabla\eta)\frac{\partial f(S)}{\partial\eta} + (v\cdot\nabla\zeta)\frac{\partial f(S)}{\partial\zeta} = 0. \tag{A.6}$$

Furthermore, it can be calculated that $(v\cdot\nabla\eta) = \lambda(S)k|\nabla\eta|^2\frac{\partial p}{\partial\eta} = \frac{|v_0|^2}{k}v_\eta$ and $(v\cdot\nabla\zeta) = \lambda(S)k|\nabla\zeta|^2\frac{\partial p}{\partial\zeta} = \frac{|v_0|^2}{k}v_\zeta$, where $|v_0| = |\nabla\psi|$ is the absolute value of the initial velocity. As for the boundary conditions, we have $p(\zeta = 0, t) = 0$, $p(\zeta = 1, t) = 1$, and zero Neumann boundary conditions on $\eta = 0$ and $\eta = \eta_0$, where η_0 represent the total flux at the initial time.

Next, we consider mapping of the permeability field into (η, ζ) coordinate system (see Fig. A.1). We assume that the flow within the channel is sufficiently high such that high flow channel is mapped into a large slab (see Fig. A.1) in (η, ζ) coordinate system. We denote by $1 - \delta(t)$ the fraction of the total flow within the channel, and assume that $\delta(t)$ remains small (for further calculations we simply denote it by δ). In the (η, ζ) coordinate system, the flow within the channel will occupy $1 - \delta$ portion of the whole domain (see Fig. A.1). Note that small δ implies some relation between the value of the permeability within the channel and the thickness of the channel. This relation can be easily obtained for simple channels. For our calculations, we only assume that the image of the channel in (η, ζ) coordinate system occupies a large slab as discussed above. Furthermore, we neglect the heterogeneities within the channel (e.g. channel's thickness in $x - y$ coordinates is small). Consequently, the saturation within the channel can be assumed to depend only on ζ at any time. In this case, the coefficients of the elliptic equation for pressure can be written as

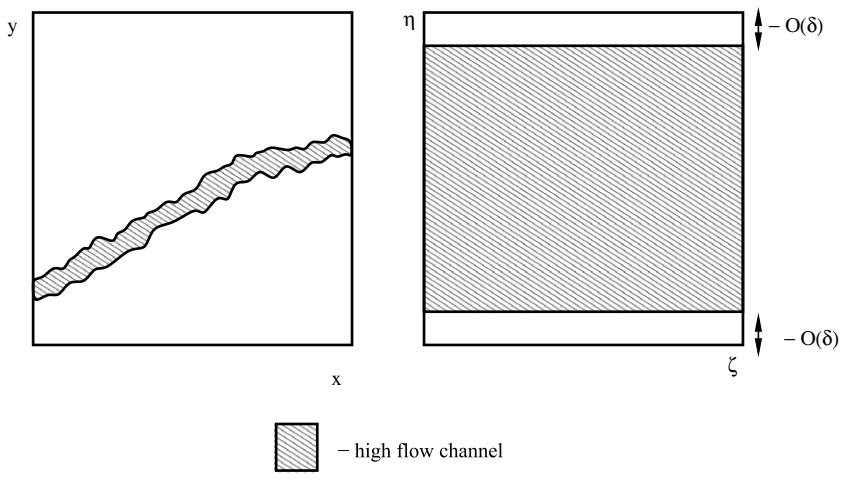

Fig. A.1. Schematic description of high flow channel and its representation in streamline-pressure coordinate system.

$$|k|^2\lambda(S) = |k_0|^2\lambda_0(\zeta,t)1_{Q_{1-\delta}} + |k_1|^2\lambda_1(\eta,\zeta,t)1_{Q_\delta}, \lambda(S) = \lambda_0(\zeta,t)1_{Q_{1-\delta}} + \lambda_1(\eta,\zeta,t)1_{Q_\delta},$$

where $Q_{1-\delta}$ denotes the region representing the channel and k_0 the permeability within this channel, and Q_δ is the outside region and k_1 the permeability outside this channel. Moreover, k_0 can be assumed to vary only along the streamline, i.e. $k_0 = k_0(\zeta)$ and is much larger than k_1. In this linear setting (when the pressure can be treated separately) one can perform formal expansion for pressure and show that

$$p(\eta,\zeta,t) = p_0(\zeta,t) + \delta p_1(\eta,\zeta,t) + \cdots, \tag{A.7}$$

where p_0 is the solution of

$$\frac{\partial}{\partial\zeta}\left(\lambda_0(\zeta,t)\frac{\partial p_0}{\partial\zeta}\right) = 0. \tag{A.8}$$

Indeed, it can be shown that $\frac{\partial}{\partial\eta}\left(|k|^2\lambda(S)\frac{\partial(p-p_0)}{\partial\eta}\right) + \frac{\partial}{\partial\zeta}\left(\lambda(S)\frac{\partial(p-p_0)}{\partial\zeta}\right) = \frac{\partial}{\partial\zeta}\left((\lambda_1(\eta,\zeta,t) - \lambda_0(\zeta,t))1_{Q_\delta}\frac{\partial p_0}{\partial\zeta}\right)$.

From here using standard estimates, one can show that $p - p_0$ is small provided δ is small. Using (A.7) one can show

$$S(\eta,\zeta,t) = S_0(\zeta,t) + \delta S_1(\eta,\zeta,t) + \cdots \tag{A.9}$$

One can also show that

$$\psi(\eta,\zeta,t) = \psi_0(\eta,t) + \delta\psi_1(\eta,\zeta,t) + \cdots$$

Rigorous justifications of these asymptotic expansions for coupled pressure and saturation equation is beyond the scope of our main goal and is currently under investigation. Note that in the asymptotic expansion presented above, we have considered linear pressure equation assuming that saturation mainly depends on ζ. The expansions (A.9) and (A.7) can be explained physically. Because the channel has high permeability, the dominant flow will be within the channel. The saturation will change in the channel rapidly (at much faster time scales compared to the saturation change outside the channel), and thus will control the pressure change in the channel. As a result, pressure will mainly vary along ζ. Note that p_0 and S_0 will vary on much faster time scales compared to other terms of the expansions.

Next, we show that the basis functions of the modified multiscale finite element method can capture $p_0(\zeta,t)$ efficiently. The asymptotic result shows that the dynamic pressure depends strongly and smoothly on the initial pressure field. Because the initial pressure field can be accurately approximated by the modified basis functions, we can show that the modified multiscale basis functions can accurately approximate the pressure field at later times. For this purpose, we need to show that the span of the modified basis functions contains an appropriate one dimensional basis. Without a loss of generality, we consider a coarse element that is on the fast flow trajectory (channel) (see Fig. A.2). Denote by $\phi_i(x)$ the modified basis functions. The pressures

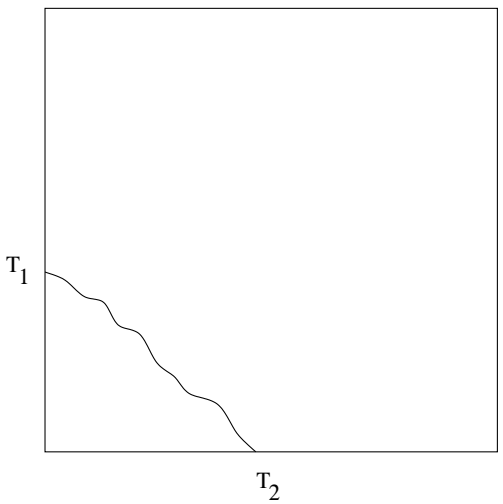

Fig. A.2. Schematic description of a streamline with a coarse block.

at the points T_1 and T_2 are different because iso-pressure lines are perpendicular to the streamline. Denote the restriction of the pressure by $p_{\text{loc}}^{\text{init}}(x)$. Consider

$$b_1(x) = \frac{p_{\text{loc}}^{\text{init}}(x) - p_{\text{loc}}^{\text{init}}(T_2)}{p_{\text{loc}}^{\text{init}}(T_1) - p_{\text{loc}}^{\text{init}}(T_2)}, \quad b_2(x) = \frac{p_{\text{loc}}^{\text{init}}(x) - p_{\text{loc}}^{\text{init}}(T_1)}{p_{\text{loc}}^{\text{init}}(T_2) - p_{\text{loc}}^{\text{init}}(T_1)}.$$

Because 1 and $p_{\text{loc}}^{\text{init}}(x)$ is in span$(\phi_1, \ldots, \phi_4)$, $b_1(x)$ and $b_2(x)$ are also in the span of ϕ_i, $i = 1, \ldots, 4$. Clearly, $b_1(x)$ and $b_2(x)$ are linear with respect to ζ, and $b_i(T_j) = \delta_{ij}$, because $p_{\text{loc}}^{\text{init}}$ is ζ. Moreover, b_1 and b_2 are linearly independent and $b_1 + b_2 = 1$. Consequently, the linear approximation of $p_0(\zeta, t)$, which is the solution of (A.8), in the span of b_1 and b_2. There is another way to show that the span of global basis in a coarse element captures $p_0(\zeta, t)$. Because the sum of the multiscale basis functions is one, the basis functions span 1. Moreover, the basis functions also span ζ because their linear combinations using the fine-scale nodal pressure values gives ζ. Thus, *1* and ζ are in the span of the global basis functions. Because $p_0(\zeta, t)$ is the solution of (A.8), it can be approximated with linear functions with respect ζ. Here, we assume S_0 is a smooth function, and consequently linear approximation of $p_0(\zeta, t)$ gives first-order accuracy (cf. (A.8)). In general, S_0 can have sharp fronts in some coarse blocks, and linear approximations will not be accurate in these coarse blocks. As we mentioned earlier, the basis functions can be updated near the front. The update of basis functions will allow us to achieve better accuracy in approximating $p_0(\zeta, t)$. As it was mentioned earlier, we have found only a very slight improvement when the basis functions are updated near the front. Here, we separate the issue of basis update near sharp interfaces from the issue of capturing of global effects with multiscale basis functions, and currently, we are investigating how the update of the basis functions may affect the accuracy of the multiscale finite element method. We see from the numerical results (e.g. Fig. 3.4) that when using the standard multiscale finite element methods, the saturation profiles are noisy and do not follow the streamlines very well. The explanation for this is that the span of the standard multiscale finite element basis functions does not contain the functions that only depend on ζ. Consequently, they can not accurately represent $p_0(\zeta, t)$. For example, we see from Fig. 3.4 that the standard multiscale finite element method introduces an artificial channel at the bottom left corner. This is because the locality of the basis functions misses the global connectivity of the media. Moreover, we observe that the boundaries of the main channel is not accurately represented by the standard multiscale basis functions, because they cannot simply span ζ. For the permeability fields generated by using two-point geostatistics with long correlation length in horizontal direction, the high permeability channels are parallel to the Cartesian coarse-grid. Since the multiscale finite element bases are linear functions along the edges of coarse-grid blocks, it can be easily shown that the span of the multiscale finite element basis functions contains the appropriate linear functions along high flow channels. Indeed, assume T_2 in Fig. A.2 is on the opposite edge and the segment (high flow channel) $[T_1, T_2]$ is parallel to horizontal axis. Then, we consider the span of the multiscale basis functions with 1 at two vertices of the edge containing T_1 and 0 at the other two vertices. The basis functions in this span accurately represent the flow along this horizontal channel. Consequently, the standard multiscale basis functions are capable of capturing channels parallel to Cartesian grids. This is one of the reasons why the multiscale finite element method works better if high permeability channels are horizontal (or vertical).

We would like to note that the above analysis is for a single-channel flow and can be extended to some more complicated flow scenarios. It is important to remark that, one does not know, in general, which channels will be active fluid carriers and the latter depends on global boundary conditions. The modified multiscale basis functions embed these global features as well as global boundary conditions into the basis functions.

References

[1] J. Aarnes, On the use of a mixed multiscale finite element method for greater flexibility and increased speed or improved accuracy in reservoir simulation, SIAM MMS 2 (2004) 421–439.

[2] T. Arbogast, Implementation of a locally conservative numerical subgrid upscaling scheme for two-phase Darcy flow, Comput. Geosci. 6 (2002) 453–481, Locally conservative numerical methods for flow in porous media.

[3] I. Babuška, G. Caloz, E. Osborn, Special finite element methods for a class of second order elliptic problems with rough coefficients, SIAM J. Numer. Anal. 31 (1994) 945–981.

[4] I. Babuška, E. Osborn, Generalized finite element methods: Their performance and their relation to mixed methods, SIAM J. Numer. Anal. 20 (1983) 510–536.

[5] J.W. Barker, S. Thibeau, A critical review of the use of pseudo-relative permeabilities for upscaling, SPE Res. Eng. 12 (1997) 138–143.
[6] F. Brezzi, Interacting With The subgrid World, In Numerical Analysis 1999, (Dundee) Chapman & Hall/CRC, Boca Raton, FL, 2000, pp. 69–82.
[7] Y. Chen, L.J. Durlofsky, M. Gerritsen, X.H. Wen, A coupled local-global upscaling approach for simulating flow in highly heterogeneous formations, Adv. Water Resour. 26 (2003) 1041–1060.
[8] Z. Chen, T.Y. Hou, A mixed multiscale finite element method for elliptic problems with oscillating coefficients, Math. Comp. 72 (2002) 541–576 (electronic).
[9] M. Christie, Upscaling for reservoir simulation, J. Pet. Tech. (1996) 1004–1010.
[10] M. Christie, M. Blunt, Tenth spe comparative solution project: a comparison of upscaling techniques, SPE Reser. Eval. Eng. 4 (2001) 308–317.
[11] C.V. Deutsch, A.G. Journel, GSLIB: Geostatistical Software Library and User's Guide, second ed., Oxford University Press, New York, 1998.
[12] L.J. Durlofsky, Numerical calculation of equivalent grid block permeability tensors for heterogeneous porous media, Water Resour. Res. 27 (1991) 699–708.
[13] L.J. Durlofsky, Coarse scale models of two phase flow in heterogeneous reservoirs: Volume averaged equations and their relationship to the existing upscaling techniques, Comput. Geosci. 2 (1998) 73–92.
[14] W. E, B. Engquist, The heterogeneous multi-scale methods, Commun. Math. Sci. 1 (1) (2003) 87–133.
[15] Y. Efendiev, T. Hou, V. Ginting, Multiscale finite element methods for nonlinear problems and their applications, Commun. Math. Sci. 2 (2004) 553–589.
[16] Y.R. Efendiev, T.Y. Hou, X.H. Wu, Convergence of a nonconforming multiscale finite element method, SIAM J. Num. Anal. 37 (2000) 888–910.
[17] T.Y. Hou, X.H. Wu, A multiscale finite element method for elliptic problems in composite materials and porous media, J. Comput. Phys. 134 (1997) 169–189.
[18] T. Hughes, G. Feijoo, L. Mazzei, J. Quincy, The variational multiscale method – a paradigm for computational mechanics, Comput. Methods Appl. Mech. Eng. 166 (1998) 3–24.
[19] P. Jenny, S.H. Lee, H. Tchelepi, Multi-scale finite volume method for elliptic problems in subsurface flow simulation, J. Comput. Phys. 187 (2003) 47–67.
[20] P. Jenny, S.H. Lee, H. Tchelepi, Adaptive multi-scale finite volume method for multi-phase flow and transport in porous media, Multiscale Model. Simul. 3 (2005) 30–64.
[21] I.G. Kevrekidis, C.W. Gear, J.M. Hyman, P.G. Kevrekidis, O. Runborg, C. Theodoropoulos, Equation-free, coarse-grained multiscale computation: enabling microscopic simulators to perform system-level analysis, Commun. Math. Sci. 1 (4) (2003) 715–762.
[22] A.-M. Matache, C. Schwab, Homogenization via p-FEM for problems with microstructure, in: Proceedings of the Fourth International Conference on Spectral and High Order Methods (ICOSAHOM 1998) (Herzliya), vol. 33, 2000, pp. 43–59.
[23] G. Sangalli, Capturing small scales in elliptic problems using a residual-free bubbles finite element method, Multiscale Model. Simul. 1 (2003) 485–503 (electronic).